Technical Note

Lattice micropatterning for cryo-electron tomography studies of cell-cell contacts

Leeya Engel [a,1], Claudia G. Vasquez [a,1], Elizabeth A. Montabana [b], Belle M. Sow [a], Marcin P. Walkiewicz [c], William I. Weis [d,e], Alexander R. Dunn [a,*]

[a] *Department of Chemical Engineering, Stanford University, Stanford, CA 94305, United States*
[b] *Stanford-SLAC CryoEM Initiative, Stanford, CA 94305, United States*
[c] *Cell Sciences Imaging Facility, Stanford University, Stanford, CA 94305, United States*
[d] *Department of Structural Biology, Stanford University School of Medicine, Stanford, CA 94305, United States*
[e] *Department of Molecular and Cellular Physiology, Stanford University School of Medicine, Stanford, CA 94305, United States*

ARTICLE INFO

ABSTRACT

Cryo-electron tomography is the highest resolution tool available for structural analysis of macromolecular complexes within their native cellular environments. At present, data acquisition suffers from low throughput, in part due to the low probability of positioning a cell such that the subcellular structure of interest is on a region of the electron microscopy (EM) grid that is suitable for imaging. Here, we photo-micropatterned EM grids to optimally position endothelial cells so as to enable high-throughput imaging of cell-cell contacts. Lattice micropatterned grids increased the average distance between intercellular contacts and thicker cell nuclei such that the regions of interest were sufficiently thin for direct imaging. We observed a diverse array of membranous and cytoskeletal structures at intercellular contacts, demonstrating the utility of this technique in enhancing the rate of data acquisition for cellular cryo-electron tomography studies.

1. Introduction

Cryo-electron tomography (cryo-ET) is a three-dimensional electron microscopy (EM) technique uniquely capable of imaging the interior of frozen cells at the nanometer scale (Asano et al., 2016; Chakraborty et al., 2020; Gan and Jensen, 2012; Medalia et al., 2002). While other EM techniques have contributed to our understanding of macromolecular organization in cells, they do not maintain macromolecules in their native states within a hydrated cell. For example, platinum replica electron microscopy is a productive technique for studying cytoskeletal organization, but it strips away the cell membrane and introduces artifacts associated with dehydration and chemical fixation (Svitkina, 2017). Preservation of cellular membranes, cytoskeletal structures and their associated proteins makes cryo-ET particularly suited to assessing the ultrastructure of cell-cell contacts (Sikora et al., 2020).

Cryo-ET is limited by the throughput of data collection, as it is time consuming to collect a sufficient number of high-quality tilt-series (Wan and Briggs, 2016). This low throughput has a number of sources, including the mechanical limitations of the stage requiring refocusing,

the software operating the microscope, and the ability to locate the region of interest. The latter issue is particularly limiting for *in situ* cryo-ET due to the challenge of identifying target complexes in the complex cellular milieu and the improbability of a cell or a subcellular region of interest being fortuitously positioned in an imageable region of the EM grid. We and others have addressed the latter limitation by applying photo-micropatterning to confine single cells to extracellular matrix (ECM) islands of predefined shapes in the centers of EM grid-squares (Engel et al., 2019; Toro-Nahuelpan et al., 2020). However, reliably positioning subcellular structures or contacts between cells remains an unmet challenge.

A longstanding challenge has been to visualize the formation and remodeling of cell-cell junctions in endothelial cells (ECs). ECs line the vasculature and actively remodel their intercellular junctions during inflammation, wound healing and vessel remodeling. Despite their critical importance to vascular health, relatively little is known about the earliest and last stages of cell-cell junction formation and disassembly, as the ultrastructure of remodeling junctions is difficult to study using conventional imaging modalities. Here, we expand on EM


grid micropatterning to facilitate cryo-ET of endothelial cell protrusions and intercellular contacts.

To image endothelial junctions by cryo-ET, we photo-micropatterned a continuous ECM lattice aligned to the EM grid that promotes the assembly of thin cell-cell contacts in imageable regions of the grid (Fig. 1). Our quantitative analysis indicates (a) that a latticework of ECM can improve the positioning of intercellular contacts relative to the EM grid and (b) that the lattice micropattern directs the thicker cell nuclei away from the centers of EM grid-squares such that cell-cell contacts can be sufficiently thin for imaging by cryo-ET. Our cryo-tomograms revealed a rich variety of sub-cellular structures in these regions, including contacting, filamentous, actin-rich membrane protrusions between cells, bundles of intersecting membrane protrusions, and a range of vesicle shapes and sizes within and outside of the plasma membrane. Lattice micropatterning of EM grids can be generalized to facilitate structural studies of a variety of other systems such as neuronal and immunological synapse formation. This study thus advances *in situ* cryo-ET by refining techniques that dramatically increase the throughput of *in situ* cryo-ET data acquisition.

2. Results and discussion

To establish an efficient pipeline for imaging endothelial cell-cell contacts by *in situ* cryo-ET, we micropatterned EM grids with a continuous lattice of ECM aligned to the grid bars. Intersections between ECM tracks attracted the thicker cell bodies while contact-forming protrusions extended along the thin, 10 μm wide regions of ECM, where they could be imaged (Fig. 1A). Using immunofluorescence, we evaluated the ability of three micropattern variations to direct cell-cell contact assembly. "Straight" micropatterns consisted of 10 μm wide intersecting tracks, while "bowtie" micropatterns consisted of 10 μm tracks that widened into 90° or 120° diamond shapes at ECM track intersections. We compared the number of cell-cell contacts on imageable regions of EM grids that were blanket-coated with ECM to the number of cell-cell contacts on imageable regions of EM grids that were micropatterned with an ECM lattice (Fig. 1B). Cell-cell contacts, indicated by the presence of vascular endothelial cadherin (VE-Cad), were observed on only 10.4 ± 4.2 (S.E.M.)% of grid-squares on EM grids that were blanket-coated with ECM (Fig. 1B, 2A). In contrast, cell-cell contacts were observed on an average of 32.4 ± 9.1 (S.E.M.)% of grid-squares for straight ECM micropatterns, 45.7 ± 5.0 (S.E.M.)% of grid-squares for 90
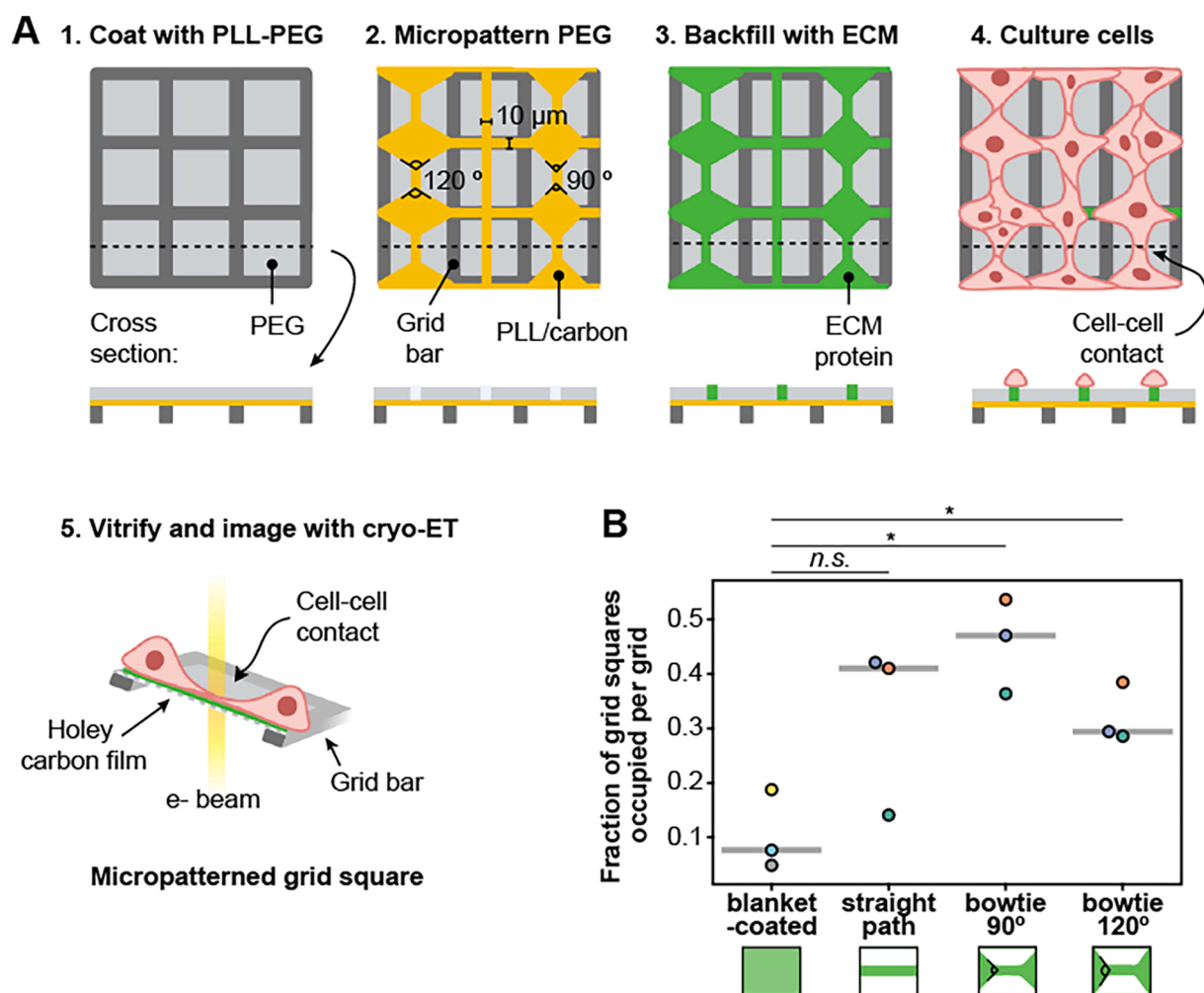
Fig. 1. Lattice micropatterning increases the number of endothelial cell-cell contacts located in imageable regions of EM grids. (A) Schematic of the lattice micropatterning method. 1. EM grids (carbon foil in yellow) undergo a PEG-PLL surface treatment (gray). 2. PEG is selectively degraded by maskless photopatterning, revealing the underlying foil (yellow). 3. Protein backfill with ECM (green). Gray regions remain PEG-coated. 4. The ECM lattice promotes the assembly of cell-cell contacts in the windows between the grid bars. (B) Lattice micropatterning increased the number of optimally positioned cell-cell junctions per EM grid. Each color represents a different EM grid. The median fraction of occupied grid squares per grid for each pattern type is indicated by the gray line. N = 3 grids that were micropatterned and 3 grids that were blanket-coated. We measured: 430 of the blanket-coated grid-squares, 108 of the 90 ° bowtie grid-squares, 108 of the 120 ° bowtie grid-squares, and 206 of the straight micropatterned grid-squares. Lines above plot indicate results of Welch's *t* tests: *P < 0.05; ns = not significant.
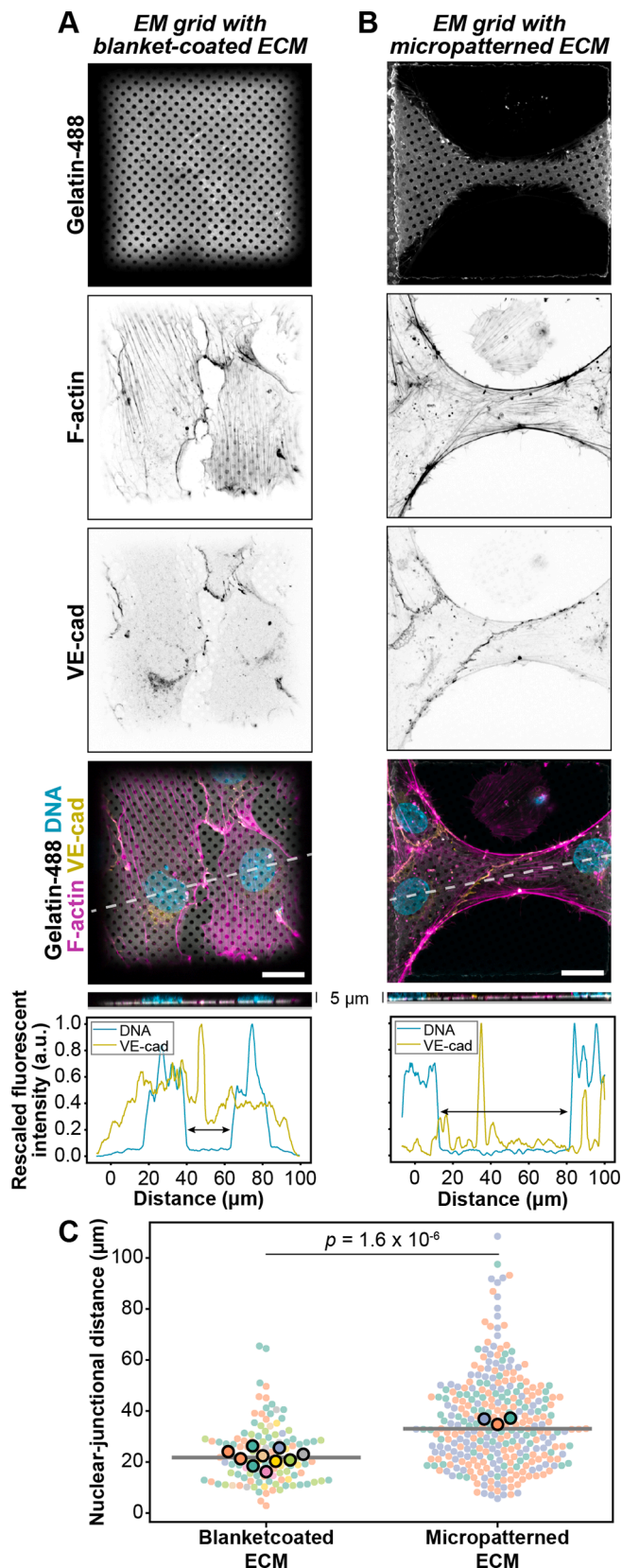
Fig. 2. Lattice micropatterning increases the distance between nuclei and cell-cell junctions in ECs cultured on EM grids. (A, B) Representative immunofluorescence image of fixed ECs on EM grids blanket-coated (A) and micropatterned (B) with Oregon Green 488-gelatin, and immunostained for F-actin, VE-cadherin (VE-cad) and DNA. The dashed line indicates the position of the Z-stack reslice and line profile of DNA (cyan) and VE-cad (green) signals. (C) Distance from nucleus center to cell-cell junction (as indicated by VE-cad signal). Each point represents an individual measurement of nuclear-junctional distance and each color represents a different EM grid. The mean of the measurements from each grid is indicated by a point outlined in black. The median for each measurement is indicated by the gray line. N = 10 grids, 120 measurements for blanket-coated condition, N = 3 grids, 320 measurements for micropatterned condition. P-value calculated using Welch's *t* test comparing grid replicates. Scale bars, 20 μm.

° bowtie micropatterns, and 32.1 ± 3.1 (S.E.M.)% for micropatterns with 120 ° bowtie micropatterns. Thus, lattice micropatterning resulted in a significant, greater than threefold increase in the instances of cell-cell contacts in imageable regions of EM grids seeded with ECs.

While previous studies in other contexts have established that cell-cell junction position can be regulated by ECM micropatterning, the nuclei of cell pairs on micropatterned ECM islands tend to be located in close proximity to the cell-cell junctions (Tseng et al., 2012; Sim et al., 2015) (Fig. S1). Cell nuclei in endothelial cells are typically several microns in height (Fig. S2). Thus, proximity of the nucleus to the cell-cell contact precludes the possibility of imaging the cell-cell contact using cryo-ET without an additional sample thinning step (Fig. S2-3). While thinning frozen cells by cryo-focused ion beam milling (cryo-FIB) is gaining traction as a preparation step for cellular cryo-ET, it requires specialized machinery that is not yet widely available and can introduce contamination or devitrification to frozen samples (Rigort et al., 2012). Moreover, cryo-FIB restricts experimental throughput due to its slow speed and complexity. Lattice micropatterning improves the likelihood of a well-positioned cell-cell contact falling below the 500 nm thickness threshold for direct imaging (Gan and Jensen, 2012) by increasing the distance between thick nuclei and intercellular junctions (Fig. 2).

We used atomic force microscopy (AFM) to examine the topography and heights of endothelial cell-cell contacts. While we observed cell-cell contacts that spanned the 10 μm width of the micropattern (Fig. 3A and S3), we also observed thinner, micron and submicron scale protrusions between cells that appeared to use the ECM micropattern as tracks for contact initiation or retraction (Fig. 3B, S4). We measured endothelial cell-cell contact heights on blanket-coated gelatin and micropatterned glass substrates. Most of the contacts measured were below the 500 nm thickness threshold and we noted that <500 nm high contacts were never wider than 10 μm for both micropatterned and blanket-coated EM grids (Fig. S6).

Lattice micropatterned EM grids generated reproducible cellular samples for cryo-ET. The grid atlas in Fig. 4A shows how lattice micropatterning can be used to orient cells (vertically or horizontally) on grid-squares, enabling the programming of visual labels for correlative EM techniques. For example, orienting cells in a single quadrant of the grid perpendicular to the direction of the cells in the other quadrants makes the location of the grid center apparent during TEM, enabling correlation with grid maps generated by light microscopy. In our hands, lattice micropatterning led to a dramatic increase in the ease of data acquisition. Once we had established optimal cell seeding density and freezing parameters, we found that we did not need to screen vitrified grids prior to imaging, as is typically required in order to identify a sufficient number of cellular subregions suitable for imaging.

Our reconstructed tomograms revealed a remarkable diversity of filamentous actin-rich membrane protrusions at cell-cell contacts (Fig. 4D-I). We observe several types of endothelial cell-cell contacts consistent with the adherens junctions described by Efimova and Svitkina (2018), namely: intercellular bridges with tip-to-tip (Fig. 4E) or lateral (Fig. 4C,D) contacts, and engulfed fingers (Fig. 4H, I). In addition,
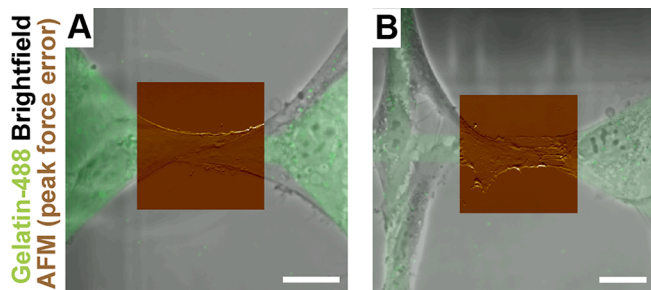
Fig. 3. Atomic force microscopy reveals the topography of endothelial cell-cell contacts. (A,B) Representative brightfield images of ECs on micropatterned glass (grayscale) overlaid with fluorescence images showing the micropattern (green). Insets show AFM peak force error scans of continuous (A) and filamentous (B) cell-cell contact phenotypes. Scale bars, 20 μm. Measurements from AFM scans show that endothelial cell-cell contact height can be below 500 nm (Fig. S6), the thickness threshold for cryo-EM samples (Gan and Jensen, 2012).

many tomograms revealed thin, intersecting membrane protrusions between cells, which appear less rigid than expected for filopodia (Fig. 4F). Their function is not immediately clear: They may be thin fibers initiating contact, retraction fibers between parting cells, migrasomes left by retreating cells (Ma et al., 2015), or suspended protrusions transferring cargo between cells, such as tunneling nanotubes (Rustom et al., 2004), which have recently been structurally analyzed by cryo-ET in neurons (Sartori-Rupp et al., 2019). Additional investigation using correlative light and electron microscopy techniques will be required to uncover the identity and function of the structures we observed. We also observed a range of vesicle shapes and sizes at endothelial cell-cell contacts (Fig. 4G-I), both within and outside of the plasma membrane.

3. Materials and methods

3.1. Cell culture

We cultured human umbilical vein endothelial cells (ECs, cat. #C2519A, Lonza Corporation, Walkdersville, MD) in EGM-2 MV Microvascular Endothelial Cell Growth Medium containing EBM-2 basal medium (Lonza cat. #CC3156) and supplemented with penicillin (50 units/mL) and streptomycin (50 μg/ml, Life Technologies, Carlsbad, CA) and the following additives from the EGM-2MV BulletKit (Lonza cat. #CC-4147): hEGFP, VEGF, hFGF-B, R3-IGF-1, hydrocortisone, and ascorbic acid and 5% FBS. We cultured cells on dishes that were pre-coated with 0.2% gelatin for > 1 h (Sigma–Aldrich, Saint Louis, MO), and maintained them at 37 °C and 5% CO_2. We used cells between passages 7 and 12.

3.2. Micropatterning

We plasma treated gold Quantifoil R 2/2 EM grids (657-200-AU, Ted Pella, Redding, CA) for 10 s at 30 W (PE-50, Plasma Etch, Carson City, NV) and incubated them in a 100 μg/ml solution of poly(l-lysine)-graft-poly(ethylene glycol)(PLL(20)-g[3.5]-PEG(2)) (SuSoS AG, Dübendorf, Switzerland) in phosphate buffered saline (PBS) for 1 h. We rinsed the grids three times in PBS and inserted them carbon-face-down into 25 μL droplets of UV-sensitive photoinitiator (PLPP, NanoscaleLABS, Fairfax, VA) contained in custom 4 mm wide silicone wells on a glass-bottom dish (Fig. S7). We then placed the dish on the stage of a Leica DMi8 outfitted with an Alvéole PRIMO maskless UV-patterning system and exposed each grid at 2500 mJ/mm^2 with the lattice micropattern (SI). We tiled the micropattern using the Leonardo software (≈22 min per 12x12 grid-square region). We rinsed the grids three times in PBS and incubated them in a 0.2% gelatin in BSA bead solution spiked with 10% by volume 1 mg/mL gelatin-Oregon Green 488 conjugate (G13186,
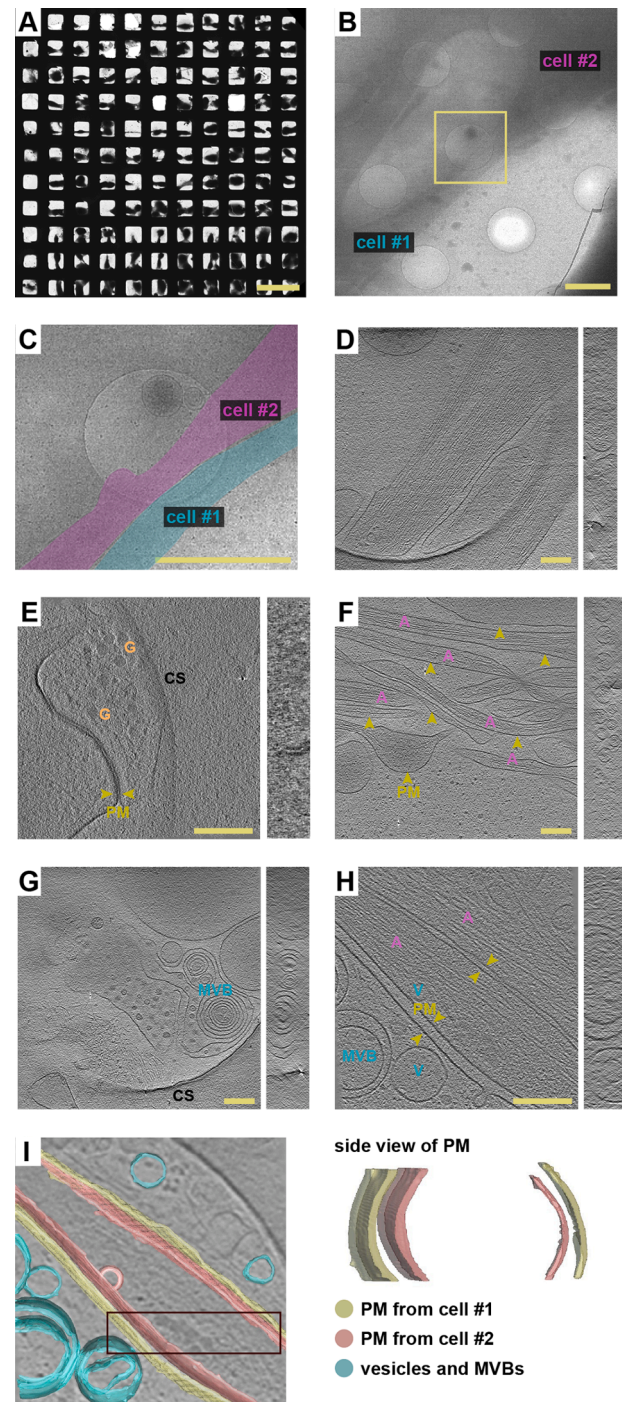
Fig. 4. Lattice micropatterning facilitates *in situ* cryo-ET of cell-cell contacts. (A) Representative cryo-TEM grid atlas of ECs adhering to a lattice micropatterned EM grid. Cells on the bottom two rows are oriented perpendicular to the cells in the above rows, as dictated by the micropattern. Such visual cues could aid correlative EM strategies. Scale bar, 200 μm. (B) Magnified cryo-TEM micrograph shows a representative region of interest for the acquisition of a tilt series (yellow box). Scale bar, 2 μm. (C) Zoomed-in image of the region in the yellow box in (B). Contacting cells were colorized for clarity. Scale bar, 2 μm. (D) Tomographic slice showing membrane-membrane interaction between cellular protrusions in (C) Scale bar, 200 nm. (E-H) Tomographic slices depict a diversity of membranous structures at cell-cell contacts. *A* actin (purple), *PM* plasma membrane (green), *V* vesicle (cyan), *MVB* multivesicular body (cyan), *G* granule (orange), *CS* carbon support. (D,E) Membrane-membrane interactions between cellular protrusions. (F) Thin, intersecting membrane protrusions. (G) Multivesicular bodies. Scale bars, 200 nm. For full tomograms, see SI. (I) Annotated membranes from (H).

Thermo-Fisher Scientific) for 1 h at $\approx$ 22 °C.

3.3. Cell seeding on micropatterned grids

To obtain the desired distribution of ECs, we suspended cells from an 80% confluent T25 at a 1:8 dilution in cell culture media. We rinsed each grid in PBS, added 10 μL of media to the carbon surface and then added 5 μL of cell suspension at a time until observing $\approx$ 2 cells/grid-square. After 2 h of incubation, we added 2 mL of warm media to each 35 mm dish and vitrified or fixed the samples after an additional 10–14 h.

3.4. Immunofluorescence and light microscopy

We fixed ECs with 4% paraformaldehyde in PBS for 15 min at $\approx$ 22 °C. We blocked and permeabilized the ECs in antibody dilution buffer (ADB) made of 0.1% Triton, 1% bovine serum albumin (BSA, Sigma) in PBS for 1 h at $\approx$ 22 °C. We incubated the ECs in a 1:500 primary antibody solution containing Mouse anti-CD144 (VE-Cad, BD Pharmingen Cat. #55561) in ADB overnight at 4 °C, and in secondary antibody solution containing Goat anti-mouse IgG Alexa Fluor 647 (Cell Signaling Technology, Cat. #4410) at a 1:1000 dilution in ADB for 1–2 h at $\approx$ 22 °C. To the latter solution we added Hoechst solution (34580, Thermo-Fisher Scientific) at a 1:1000 dilution to identify nuclei and ActinRed 555 Red Probes reagent (R37112, Thermo-Fisher Scientific) at 1 drop/ mL to stain F-actin. Images in Fig. 2A-B were acquired using an inverted Zeiss LSM 780 confocal microscope with a 40X/1.3 NA C-Apo water objective and using Zen Black software (Carl Zeiss). Images used for Fig. 1B, 2C, and S1 were acquired on an inverted Nikon Ti-E microscope equipped with a Heliophor light engine (89 North) and an Andor sCMOS Neo camera using a 20x Plan Apo Lambda air objective lens. Nuclear-junctional distances were measured using ImageJ (Fig. S8,S9) (Schneider et al., 2012).

3.5. Atomic force microscopy

We performed atomic force microscopy (AFM) on live and fixed cells cultured on glass bottom dishes using a BioScope Resolve BioAFM in PeakForce QNM mode and a PFQNM-LC-A-CAL cantilever (Bruker, Santa Barbara, CA). We did not perform AFM on cells cultured on EM grids due to the delicate and porous nature of the carbon thin films. There were no discernable differences in cell morphology on micropatterned glass and EM grids (Fig. 3A-B, 2A-B, A-B, S2-S4, and S6). We measured cell-cell contact heights of cells cultured on blanket coated and micropatterned glass bottom dishes with the height sensor channel using Nanoscope Analysis 1.9 (Fig. S6). The AFM was mounted on a Zeiss Axio Observer Z1 inverted epifluorescent microscope outfitted with a 20x objective.

3.6. Vitrification, cryo-ET, and tomogram reconstruction

We added 3 μL of AuNP solution to each grid (Aurion BSA Gold tracer 10 nm, Fisher Cat. #50-248-12) before vitrifying the grids in a Leica EM GP plunge freezer. We clipped the grids into autogrids and loaded them into an FEI Krios G2 transmission electron microscope (TEM) equipped with an energy filter and a K2 direct electron detector (Gatan). We used SerialEM software (Mastronarde, 2005) to operate the TEM at 300 kV in low-dose mode and acquire tilt series at a magnification of 33,000x (0.4315 nm/px) (Fig. 4 D,F,and G) and at a magnification of 64,000x (0.2235 nm/px), using a Volta phase plate to improve image contrast (Fig. 4 E and H) (Danev et al., 2014). Tilt series were acquired with 2° steps between −60° and +60° and a defocus range between −2 μm and −5 μm. We motion corrected images with MotionCor2 software (Zheng et al., 2017), aligned them using gold fiducials, and reconstructed tomograms using the IMOD software package, version 4.9.1 (Kremer et al., 1996). 3D reconstructions were calculated using the weighted-back projection using IMOD (Kremer et al., 1996). We segmented the tomogram volume in Fig. 4I using Amira (FEI/Thermo Fisher Scientific) software.

Author Contributions

L.E., C.G.V., W.I.W., and A.R.D. designed research; L.E., C.G.V., E.A. M., B.M.S. and M.P.W. performed research and analyzed data; L.E. and C.G.V. wrote the paper; A.R.D and W.I.W. edited the paper.

CRediT authorship contribution statement

Leeya Engel: Conceptualization, Methodology, Investigation, Writing - original draft, Formal analysis, Visualization, Project administration. **Claudia G. Vasquez:** Conceptualization, Methodology, Software, Investigation, Writing - original draft, Formal analysis, Data curation, Visualization, Project administration. **Elizabeth A. Montabana:** Resources. **Belle M. Sow:** Formal analysis. **Marcin P. Walkiewicz:** Resources. **William I. Weis:** Writing - review & editing, Supervision. **Alexander R. Dunn:** Conceptualization, Writing - review & editing, Supervision, Project administration, Funding acquisition.

Declaration of Competing Interest

The authors declare that they have no known competing financial interests or personal relationships that could have appeared to influence the work reported in this paper.

Acknowledgements

Appendix A. Supplementary data

Supplementary data associated with this article can be found, in the online version, at https://doi.org/10.1016/j.jsb.2021.107791.

References

Asano, S., Engel, B.D., Baumeister, W., 2016. In situ cryo-electron tomography: a post-reductionist approach to structural biology. J. Mol. Biol. 428 (2), 332–343.

Chakraborty, S., Jasnin, M., Baumeister, W., 2020. Three-dimensional organization of the cytoskeleton: A cryo-electron tomography perspective. Protein Sci. 29 (6), 1302–1320.

Efimova, N., Svitkina, T.M., 2018. Branched actin networks push against each other at adherens junctions to maintain cell–cell adhesion. J. Cell Biol. 217 (5), 1827–1845.

Danev, R., Buijsse, B., Khoshouei, M., Plitzko, J.M., Baumeister, W., 2014. Volta potential phase plate for in-focus phase contrast transmission electron microscopy. Proc. Natl. Acad. Sci. U. S. A. 111 (44), 15635–15640.

Engel, L., Gaietta, G., Dow, L.P., Swift, M.F., Pardon, G., Volkmann, N., Weis, W.I., Hanein, D., Pruitt, B.L., 2019. Extracellular matrix micropatterning technology for whole cell cryogenic electron microscopy studies. J. Micromech. Microeng. 29 (11), 115018.

Gan, L., Jensen, G.J., 2012. Electron tomography of cells. Q. Rev. Biophys. 45 (1), 27–56.

Kremer, J.R., Mastronarde, D.N., McIntosh, J.R., 1996. Computer visualization of three-dimensional image data using IMOD. J. Struct. Biol. 116 (1), 71–76.

Ma, L., Li, Y., Peng, J., Danni, W., Zhao, X., Cui, Y., Chen, L., Yan, X., Du, Y., Yu, L., 2015. Discovery of the migrasome, an organelle mediating release of cytoplasmic contents during cell migration. Cell Res. 25 (1), 24–38.

Mastronarde, D.N., 2005. Automated electron microscope tomography using robust prediction of specimen movements. J. Struct. Biol. 152 (1), 36–51.

Medalia, O., Weber, I., Frangakis, A.S., Nicastro, D., Gerisch, G., Baumeister, W., 2002. Macromolecular architecture in eukaryotic cells visualized by cryoelectron tomography. Science 298 (5596), 1209–1213.

Rigort, A., Bäuerlein, F.J.B., Villa, E., Eibauer, M., Laugks, T., Baumeister, W., Plitzko, J.M., 2012. Focused ion beam micromachining of eukaryotic cells for cryoelectron tomography. Proc. Natl. Acad. Sci. U. S. A. 109 (12), 4449–4454.

Rustom, A., Saffrich, R., Markovic, I., Walther, P., Gerdes, H., 2004. Nanotubular highways for intercellular organelle transport. Science 303 (5660), 1007–1010.

Sartori-Rupp, A., Cordero Cervantes, D., Pepe, A., Gousset, K., Delage, E., Corroyer-Dulmont, S., Schmitt, C., Krijnse-Locker, J., Zurzolo, C., 2019. Correlative cryo-electron microscopy reveals the structure of TNTs in neuronal cells. Nat. Commun. 10 (1), 1–16.

Schneider, C.A., Rasband, W.S., Eliceiri, K.W., 2012. NIH Image to ImageJ: 25 years of image analysis. Nat. Methods 9 (7), 671–675.

Sikora, M., Ermel, U.H., Seybold, A., Kunz, M., Calloni, G., Reitz, J., Vabulas, R.M., Hummer, G., Frangakis, A.S., 2020. Desmosome architecture derived from molecular dynamics simulations and cryo-electron tomography. Proc. Natl. Acad. Sci. U. S. A. 117 (44), 27132–27140.

Sim, J.Y., Moeller, J., Hart, K.C., Ramallo, D., Vogel, V., Dunn, A.R., Nelson, W.J., Pruitt, B.L., 2015. Spatial distribution of cell–cell and cell–ECM adhesions regulates force balance while maintaining E-cadherin molecular tension in cell pairs. Mol. Biol. Cell 26 (13), 2456–2465.

Svitkina, T.M., 2017. Platinum replica electron microscopy: Imaging the cytoskeleton globally and locally. Internatl. J. Biochem. Cell Biol. 86, 37–41.

Toro-Nahuelpan, M., Zagoriy, I., Senger, F., Blanchoin, L., Théry, M., Mahamid, J., 2020. Tailoring cryo-electron microscopy grids by photo-micropatterning for in-cell structural studies. Nat. Methods 17 (1), 50–54.

Tseng, Q., Duchemin-Pelletier, E., Deshiere, A., Balland, M., Guillou, H., Filhol, O., Théry, M., 2012. Spatial organization of the extracellular matrix regulates cell–cell junction positioning. Proc. Natl. Acad. Sci. U. S. A. 109 (5), 1506–1511.

Wan, W., Briggs, J.A.G., 2016. Cryo-electron tomography and subtomogram averaging. In: Crowther, R.A. (Ed.), Methods in Enzymology, 579. Academic Press, pp. 329–367.

Zheng, S.Q., Palovcak, E., Armache, J.P., Verba, K.A, Cheng, Y., Agard, D.A., 2017. Motioncor2: Anisotropic correction of beam-induced motion for improved cryo-electron microscopy. Nat. Methods 14 (4), 331–332.